Geophysical Journal International

Geophys. J. Int. (2020) **223,** 777–791
Advance Access publication 2020 August 06
GJI Seismology

doi: 10.1093/gji/ggaa326

Seismicity induced by massive wastewater injection near Puerto Gaitán, Colombia

I. Molina [1,*] J.S. Velásquez,[1,†] J.L. Rubinstein,[2] A. Garcia-Aristizabal [3] and V. Dionicio[1]

[1] *Servicio Geológico Colombiano-SGC, Diagonal* 53 *No* 34–53, *Apartado Aéreo* 4865, *Bogotá, Colombia*
[2] *United States Geological Survey—USGS,* 345 *Middlefield Road/MS-*977, *Menlo Park CA* 940225, *USA*
[3] *Istituto Nazionale di Geofisica e Vulcanologia, Sezione di Bologna, via Donato Creti* 12, 40128 *Bologna, Italy*

Accepted 2020 June 30. Received 2020 May 9; in original form 2019 October 4

SUMMARY

Seven years after the beginning of a massive wastewater injection project in eastern Colombia, local earthquake activity increased significantly. The field operator and the Colombian Geological Survey immediately reinforced the monitoring of the area. Our analysis of the temporal evolution of the seismic and injection data together with our knowledge of the geological parameters of the region indicate that the surge of seismicity is being induced by the re-injection of produced water into the same three producing reservoirs. Earthquake activity began on known faults once disposal rates had reached a threshold of $\sim 2 \times 10^6$ m^3 of water per month. The average reservoir pressure had remained constant at 7.6 MPa after several years of production, sustained by a large, active aquifer. Surface injection pressures in the seismically active areas remain below 8.3 MPa, a value large enough to activate some of the faults. Since faults are mapped throughout the region and many do not have seismicity on them, we conclude that the existence of known faults is not the only control on whether earthquakes are generated. Stress conditions of these faults are open to future studies. Earthquakes are primarily found in four clusters, located near faults mapped by the operator. The hypocentres reveal vertical planes with orientations consistent with focal mechanisms of these events. Stress inversion of the focal mechanisms gives a maximum compression in the direction ENE-WSW, which is in agreement with borehole breakout measurements. Since the focal mechanisms of the earthquakes are consistent with the tectonic stress regime, we can conclude that the seismicity is resulting from the activation of critically stressed faults. Slip was progressive and seismic activity reached a peak before declining to few events per month. The decline in seismicity suggests that most of the stress has been relieved on the main faults. The magnitude of a large majority of the recorded earthquakes was lower than 4, as the pore pressure disturbance did not reach the mapped large faults whose activation might have resulted in larger magnitude earthquakes. Our study shows that a good knowledge of the local fault network and conditions of stress is of paramount importance when planning a massive water disposal program. These earthquakes indicate that while faults provide an opportunity to dispose produced water at an economically attractive volume–pressure ratio, the possibility of induced seismicity must also be considered.

Key words: Fracture and flow; Earthquake dynamics; Earthquake source observations; Induced seismicity.

1 INTRODUCTION

We study the seismicity in the adjacent and contiguous Rubiales and Quifa oil fields of eastern Colombia, which dramatically increased in 2013 July and 2014 January, respectively (Fig. 1a; see also a movie in Appendix A in the online version). Production in these oil

* Now at: Universidad de los Andes, Cra 1 No 18 A 12, Apartado Aéreo 111711, Bogotá, Colombia. E-mail: ci.molina@uniandes.edu.co
† Now at: Seismology Research Centre, 141 Palmer Street, Richmond VIC 3121, Australia

Published by Oxford University Press on behalf of The Royal Astronomical Society 2020. This work is written by (a) US Government employee(s) and is in the public domain in the US.

Downloaded from https://academic.oup.com/gji/article/223/2/777/5881935 by guest on 07 September 2020

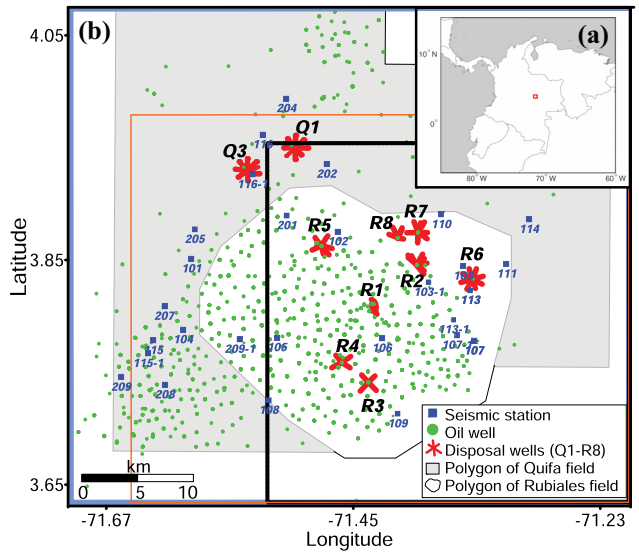

Figure 1. Location of seismic stations, oil wells and wastewater disposal wells: (a) map location of the zone of study in Colombia shown as a red square in inset. (b) Pads of disposal wells and seismic stations. The SGC seismic station is not shown on the map because it is approximately 50 km from the seismic clusters. Green dots represent the oil wells, pads of disposal wells are indicated in red and seismic stations as blue squares. Lines spreading from disposals wells represent the horizontal sections. Polygon area shows the region in which automatic detections were made in the operator catalogue for periods 2013 July–2014 January (dotted black line), from 2014 January to July (orange line) and from 2014 August to 2016 June (blue line). Note that pad Q3 is outside and Q1 is on the edge of the automatic detection zones for the first period of the operator catalogue.

fields, started respectively, in 1997 and 2009, whereas significant water injection initiated in 2010 February and 2012 January. The water cut (the percentage of water in the total produced volume) increased to reach over about 95 per cent. Nearly all of the produced water is re-injected into the same formation from where the oil is extracted. Re-injection at Quifa occurs southwest of the producing area and predominantly east of the producing area at Rubiales. This massive scale injection is done in the same producing Carbonera formations between a depth of 0.51 and 0.85 km. Considering both Quifa and Rubiales fields, approximately 7×10^5 m^3 of wastewater are injected daily through 70 wells drilled in two locations (or pads) in Quifa and eight locations in Rubiales (Fig. 1b). The studied earthquake sequence includes eight $M \geq 4$ earthquakes, with the largest earthquake being an M 4.5 in 2015. Seismicity rates declined in recent years, from a peak rate of six $M \geq 3$ earthquakes per day in 2015 to one $M \geq 3$ earthquake in 2016. Given the proximity of the seismicity to the oil field, a previous study of the seismicity in this area suggested that this seismicity may have been induced by hydrocarbon production operations (Gómez-Alba *et al.* 2015, 2020).

Globally, most earthquakes are tectonic in origin, but under some geologic and reservoir conditions, underground injection of wastewater can induce seismicity. Numerous studies have been conducted to understand the influence of fluid injection on seismicity (e.g. Evans 1966; Healy *et al.* 1968; Raleigh *et al.* 1976; Lei *et al.* 2008; Ellsworth 2013; Rubinstein *et al.* 2014). Studies typically argue that increased pore pressure is responsible for inducing the earthquakes, although there is evidence that poroelastic stresses are also important (Barbour *et al.* 2017). Induced earthquakes typically occur close to the injection formation within the crystalline basement, 1–10 km below the surface of the Earth (Keranen *et al.* 2014; Stabile *et al.* 2014; Yeck *et al.* 2016; Rubinstein *et al.* 2018).

In this study, we focus our attention on the spatial and temporal relationships between injection parameters and seismicity in the Quifa and Rubiales fields; our main objective is to understand if and how the seismicity was induced. We also analyse the orientation of the faults on which the earthquakes are occurring to determine whether they are critically stressed. We show how seismicity dramatically increased one month after the wastewater injection rate reached a level that we propose to be a critical threshold. The earthquake hypocentres spread over a limited area, constrained by identified faults, progressively reaching deeper formations until seismicity almost stopped once the stress was relieved. This provides clear evidence of a diffusive signature to the seismicity.

2 GEOLOGICAL SETTING AND OPERATIONAL PARAMETERS

The Rubiales and Quifa oil fields are located in the southeast of the Llanos Basin, 250 km SE from Villavicencio, capital of the state of Meta, Colombia. It is one of the most productive heavy oil fields in the country. (Table A1 in Appendix B). Geologically, Rubiales oil field is an extensive monocline trending NNE and dipping 1°–2° to the NW. It is located in a typical foreland basin associated with the Eastern Cordillera, where—from top to the bottom of stratigraphic column—neogene sediments (Necesidad, Guayabo, León, and Carbonera Formations) lie unconformably over the palaeozoic and precambrian (basement) rocks of the Guyana Shield (Cooper *et al.* 1995; Gómez *et al.* 2010; INGRAIN & ANH 2012; Dasilva *et al.* 2013). The basin is a product of extensional deformation generated by the tectonic load of the Eastern Cordillera (Gómez *et al.* 2010). In the Rubiales area, 3-D seismic interpretation indicates the presence of mostly vertical faults of variable length, with little vertical displacement, most of them of 3–6 m (Gómez *et al.* 2010).

The oil reservoir is located in the lower sandstones of the Carbonera Formation, operationally called 'basal sandstones'. These sandstones are mainly a consequence of fluvial environment deposits of braided rivers during the late Eocene—early Oligocene. The sand bodies appear stratified with very fine-grained rocks resulting from flooded plains deposits, which has created a very complex stratigraphy. A tilted oil-water contact was identified while drilling. According to Gómez *et al.* (2010), this contact can be related to the presence of a hydrodynamic trap, large enough to sustain a constant reservoir pressure of ∼7.6 MPa in spite of the high volume of oil produced so far, as well as its coherence with the structural reservoir dip.

The water cut in the field reached 96 per cent in 2016. This requires the daily injection of $\sim 7 \times 10^5$ m^3 of wastewater through two sets of wells at field Quifa (pads Q1 and Q3) and eight pads at Rubiales (R1–R8, Fig. 1b). Wastewater is injected into three different horizons: Carbonera C1 (∼0.51–0.57 km below surface), Carbonera Intermediary (∼0.55–0.61 km below surface) and Carbonera basal sandstones (depth of ∼0.7–0.85 km below surface), with the majority of injection into the basal sandstones, which is also the production formation. Thus, injection is either above or within the production formation. While injection into a production formation is commonly undertaken to support a secondary recovery process, the stratigraphic and structural complexity led the operator to place the injection wells to the NE of the production area (Fig. 1b) and

Downloaded from https://academic.oup.com/gji/article/223/2/777/5881935 by guest on 07 September 2020

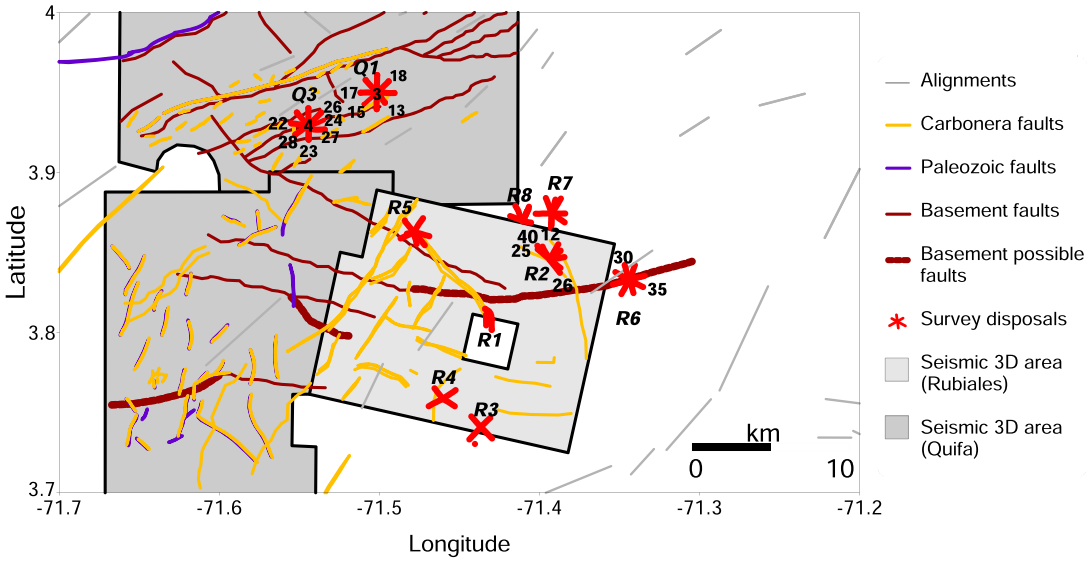

Figure 2. Faults and alignments in relation with pads and areas of seismic surveys. Some wells at pad Q1, Q3, R2, R6, R7 and R8 are numbered and referenced in the text.

they are not intended to improve oil extraction. The sedimentary–cyrstalline basement contact in the area ranges from 1 to 1.8 km depth.

3 DATA

3.1 Geological and operational data

The field operator Pacific Rubiales Energy (Meta Petroleum Corporation) provided the injection rates and the surface pressure data. The operator obtained the geological structures and a detailed fault map of the complex oil fields through the processing of dense 2-D and 3-D seismic surveys; such data is summarized in Fig. 2. Furthermore, using aerial photographs, the Colombian Geological Survey (SGC) identified topographic lineaments may be indicative of additional faults, primarily outside the area where the 3-D surveys were performed (Fig. 2).

3.2 Seismic networks

When the wastewater injection started in 2007 November, the closest existing seismological station was located approximately 200 km from the study area. This station was installed in 1993 as part of the National Seismic Network of Colombia, which is administered by the SGC. Given the distance of the station to the area of interest, we were not able to establish a reliable estimate of the background rate of naturally occurring earthquakes for magnitudes $M \leq 3$. Only two events, an M 3 in 1997 July and an M 2.3 in 2012 September, were recorded in the zone of Puerto Gaitán prior to the intense activity of 2013. Based on the population in this region, we typically expect earthquake felt reports for earthquakes as small as M 3. However, there were no felt earthquake reports between 1993 and 2013 March, so we can reasonably assume that no earthquakes larger than 3 occurred during this time period. In 2013 April, SGC detected the increase in seismicity that we study in this work.

After seismicity was reported in 2013 March, the operator installed a 28-station seismic network (Fig. 1b) that remained in use between 2013 and 2016 July. The stations were gradually deployed and moved around to optimize the monitoring of the seismic activity of both Rubiales and Quifa fields (Appendix A). Recording stopped in 2016 July, when another entity started to operate the field. In 2013 September, the SGC installed a seismometer at ∼60 km from Puerto Gaitan to improve the coverage of the existing national seismic network. The other stations of SGC were located further than 60 km from seismic clusters.

3.3 Earthquake catalogues

Two seismic catalogues were available for this study: one produced by the SGC and another produced by the field operators. We first analyse the consistency of both catalogues and determine their completeness magnitude (M_c) using, comparatively, three methods [namely the Maximum Curvature, the Goodness of Fit (Wiemer & Wyss 2000), and the Modified Goodness of Fit (Leptokaropoulos *et al.* 2013)], which are available in the EPOS (European Plate Observing System) platform for anthropogenic hazards (EPOS-AH, Orlecka-Sikora *et al.* 2020).

Merging waveforms of SGC and operator catalogues was unsatisfactory since the *P*-wave onset arrival at the SGC stations were of insufficient quality. The operator processed the data recorded by their network using a migration-based methodology, producing a catalogue of 29 629 events between 2013 and 2016 July, with an M_c of 1.1, calculated by using the maximum curvature approach (Wiemer & Wyss 2000, see Appendix B for details). Locations, moment magnitudes and waveforms for these earthquakes were made available.

The SGC established a catalogue of 1064 events recorded by the National seismic network between 2012 September and 2016 July and using a 1-D regional velocity model developed for the entire country. The resulting SGC magnitudes ranged from 1.2 to 4.8, with an M_c of 2.4 by using the maximum curvature approach (Wiemer & Wyss 2000). Given large location errors in the original SGC catalogue (7 km horizontally and 10 km in depth), we develop a new catalogue using the SGC catalogue and operator's network. We first select the 169 $M \geq 3.0$ earthquakes in the SGC catalogue from 2013 August to 2016 January. Then, we extract 1-hr window

Downloaded from https://academic.oup.com/gji/article/223/2/777/5881935 by guest on 07 September 2020

around each selected earthquake for every station available from the operator's network. Finally, we manually search and pick *P* and *S* arrivals for all visible local events within the 1-hr window around each $M \geq 3.0$ event from all stations. As a result, the reprocessed catalogue includes 1616 earthquakes, 1447 of which were added by manual inspection. By construction, the resulting SGC reprocessed catalogue has a nominal completeness of $M_c = 3.5$ (even though that it can be considered complete for magnitudes above 3.3 according to the modified goodness of fit method, Leptokaropoulos *et al.* 2013). Magnitudes from the operator's catalogue range from −0.5 to 4.5 (Fig. A1e in Appendix B), while that of SGC reprocessed data ranged from −0.6 to 4.2.

4 METHODOLOGY

4.1 Development of a new source of information

We used the information from both the reprocessed SGC catalogue (1616 events) and the operator's catalogue above $M_c = 1.1$ (15343 events). The reprocessed SGC catalogue was used to (i) produce a new velocity model and to relocate the earthquakes using this new velocity model (Figs A1b–d and details in Appendix B), (ii) establish a new formula to calculate the magnitude (Figs A1e–h, Table A2 and details in Appendix B) and (iii) to determine focal mechanisms and invert for stress (Tables A3 and A4, and details in Appendix B). The locations of events in the SGC reprocessed catalogue were recorded on at least seven stations within 6 km and the uncertainties were 0.4 km horizontally and 0.8 km in depth, while the location uncertainties for the operator's catalogue were 0.02 km horizontally and 0.05 km in depth, however only events at depths ≤ 7 km were reported, so any seismicity below this depth was not included. We used the operator's catalogue for a detailed description of the earthquake spatial-temporal evolution (locations and number) while the SGC's reprocessed catalogue was used to confirm the presence of any seismicity deeper that 7 km depth.

A new M_L relationship was derived based on SGC reprocessed catalogue:

$$M_L = \log A + 1.02 \log(r) + 0.022r - 2.31 + S \quad (1)$$

where *A* is the peak-to-peak amplitude measured in mm, *r* is the hypocentral distance in km and *S* is the station correction. This equation provides less dispersion of magnitudes than the initial SGC formulation (details in Appendix B), and is used to obtain new M_L estimates for the 1616 events in the reprocessed SGC catalogue, including those newly added events. The operator's M_w magnitudes are on average 1.6 units smaller than the SGC's estimates, and 0.8 units smaller than the M_b computed for larger earthquakes detected by the USGS. Since operator's M_w magnitude is deemed unreliable, only the new derived *ML* for the SGC catalogue is used for later analysis.

4.2 Determining material properties

First, we are interested in measuring the hydraulic diffussivity in the study area. In a homogeneous and isotropic medium, the size of the relaxation zone (i.e. a spatial domain of physical changes) can be described by the following equation for the triggering front (Shapiro *et al*. 1997, 2002):

$$R_t = \sqrt{4\pi Dt} \quad (2)$$

Where *t* is the time elapsed since the injection start, *D* is the scalar hydraulic diffusivity and R_t is the radius of the triggering front (i.e. the extent to which pore-pressure perturbations are expected). To estimate diffusivity, we calculate the distances r_i between an injection point and the *i*th earthquake (belonging to a same cluster), and plot them against the time elapsed between the event occurrence and the start of injection, t_i (for earthquakes in the same cluster (e.g. Shapiro *et al.* 1997). These data (i.e. time from the start of the injection and the relative maximum distance reached by seismicity), are used to determine the diffusivity according to eq. (2). The inference of the diffusivity is performed using a Markov Chain Monte Carlo (MCMC) method following an approach as the one described by Garcia-Aristizabal *et al.* (2016).

Permeability can be used to estimate hydraulic conductivity *K* as follows (Schwartz & Zhang 2003):

$$K = \frac{k\rho g}{\mu} \quad (3)$$

Where *k* is the permeability, ρ is the pore fluid density, *g* is the gravity constant and μ is the pore fluid viscosity. Hydraulic conductivity and diffusivity can be related through the permeability as $D = K/\rho g S$ (Biot 1956 ; Rice & Clearly 1976; Van der Kamp & Gale 1983), where *S* is the storage coefficient of the rock which depends on the poroelastic medium properties. Since *D* and *S* properties were not readily available from the operator, we used the two above equations independently.

4.3 Implementation of an injection index

In a semi-confined reservoir, the injection pressure is directly proportional to the increase in injection rate. For each well, we calculated an injection index defined as injectivity (Goebel & Brodsky 2018), the ratio between injection rate and injection pressure**:**

$$\text{Inj Index} = \frac{i_r}{i_p} \quad (4)$$

where i_r is the injection rate (in $m^3\,d^{-1}$) and i_p is the injection pressure (in MPa). We use the injection index to evaluate if the continuous variations of flow rate due to operational constraints results in a similar variation in associated injection pressure. Significant variations of this index may result from a change in the flow parameters of the medium, such as a change in permeability.

4.4 Determination of local stress field

We computed focal mechanisms by using the method described in Reasenberg & Oppenheimer (1985). In total, we obtained focal mechanisms for 48 events with errors in the strike, dip and rake that do not exceeded 5°, and with a minimum and average number of *P*-wave polarities of 7 and 15, respectively. However, to analyse the local stress field in the study area, we selected the best focal mechanisms available with a minimum number of *P*-wave polarities of 16, an STDR ≥ 0.40 (Station Distribution Ratio, as Bailey *et al.* 2010) and a misfit polarity average of 0.0 (details in Table A3 in Appendix B). This analysis was performed using the STRESSINVERSE code of Vavryčuk (2014), a modification of the method developed in Michael (1987).

Downloaded from https://academic.oup.com/gji/article/223/2/777/5881935 by guest on 07 September 2020

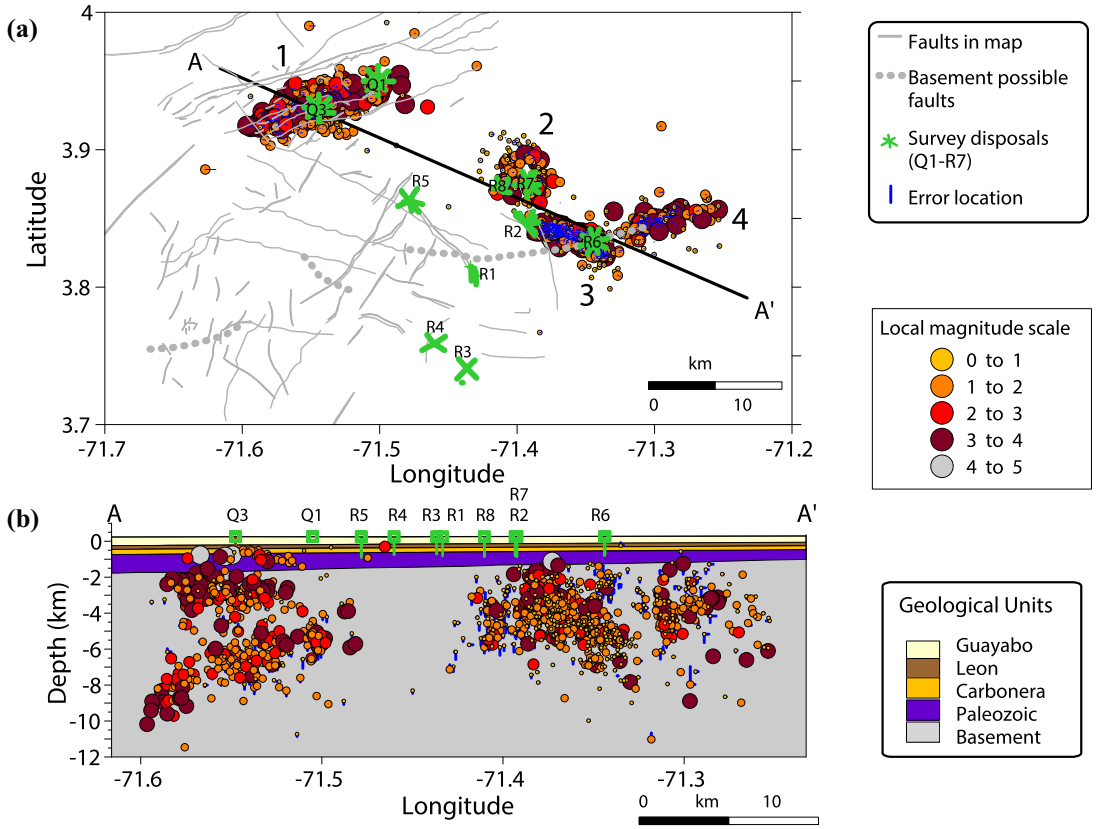

Figure 3. (a) Map of seismicity from SGC catalogue overlapped to mapped faults interpreted by operator. (b) Cross-section along the different clusters crossed with the geology. Cross-section has a width of 5 km. The earthquakes are displayed with both colour-coded and size (radius) related to a local magnitude scale. Stratigraphic information is only an approximation of the geology of the zone (e.g. Pacific Rubiales Energy 2009; Gómez *et al.* 2010).

5 RESULTS

The SGC reprocessed catalogue showed that seismicity was concentrated in four clusters around pads Q1–Q3, R7–R8, R6 towards NE, and between R6 towards R2 (Fig. 3a); they will be referred to as clusters 1, 2, 3 and 4 respectively from hereon. Depths range from 1 to 12 km (Fig. 3b). We find a clear correlation in space between the clusters 1, 2 and 4, the planes of seismicity and the previously mapped faults (Fig. 3). These clusters were delineated by applying a classical partitioning approach based on the *k*-means method (MacQueen 1967; details in Appendix C) to the operator's catalogue (Fig. 4a). The earthquakes related to pads Q1–Q3 formed cluster 1 and those related to pads R7–R8 formed cluster 2. Since injection rates and pressures vary from pad to pad, the frontier between two zones of influence is not well defined. As such, seismicity near the edges of the clusters does not always clearly belong on cluster or another. We enclosed with an ellipse the earthquakes from R6 toward NE (cluster 3), and those from R6 towards R2 (cluster 4). The seismicity in clusters 1, 3 and 4 spans vertically along faults mapped by the field operator (Fig. 4a), crossing the León, Carbonera, palaeozoic and basement formations (Figs 4b–e; unpublished data shared by the operator). In cluster 4, we observe two alignments of earthquakes at surface toward the NE and at depth, crossing the palaeozoic and probably the upper formations (details in Appendix C). This suggests a downward migration of fluid pressure perturbation inducing these earthquakes. In contrast, hypocentres related to cluster 2 appear to be generally deep ($>$ 3 km) without suggesting a structural fabric (Figs 4a and c). Despite the fact that the operator reported uncertainties in depth of 0.05 km, we think that the relatively poor seismic coverage (compare Figs 1 and 4) and the lack of 3-D seismic data (compare Figs 2 and 4) for this area does not allow us to accurately constrain depths, nor can we correlate the seismicity with known faults.

5.1 Quifa

5.1.1 Description of seismicity, flow rate and injection pressure

Waste water injection started at pad Q1 in 2012 January and at pad Q3 in 2012 October. The seismic network was installed 4–6 months before the start of the seismic activity in Quifa, in 2014 January. The combined set of earthquake and injection (rate and pressure) data were then available from the beginning of the earthquake activity, allowing us to establish a reliable relationship between injection and seismicity over the entire time of our study.

There is a clear correlation between the rise in seismicity and the injection activities (Fig. 5). The first recorded earthquakes occurred in 2014 January when the volume injected at pad Q3 reached 2.2×10^6 m^3 (Fig. 5a) and the associated injection pressure reached an average of 6.2 MPa (Fig. 5b). The intense seismic activity lasted 10 months: 98 per cent of the 3039 earthquakes recorded in this zone from 2014 January to 2016 April occurred between 2014 January and 2015 May. Activity progressively declined to an average of four events per month between 2015 June and 2016 April. We find that the seismicity resulting from the reactivation of the faults decreased after releasing pre-existing tectonic stress. The hypocentres below

Downloaded from https://academic.oup.com/gji/article/223/2/777/5881935 by guest on 07 September 2020

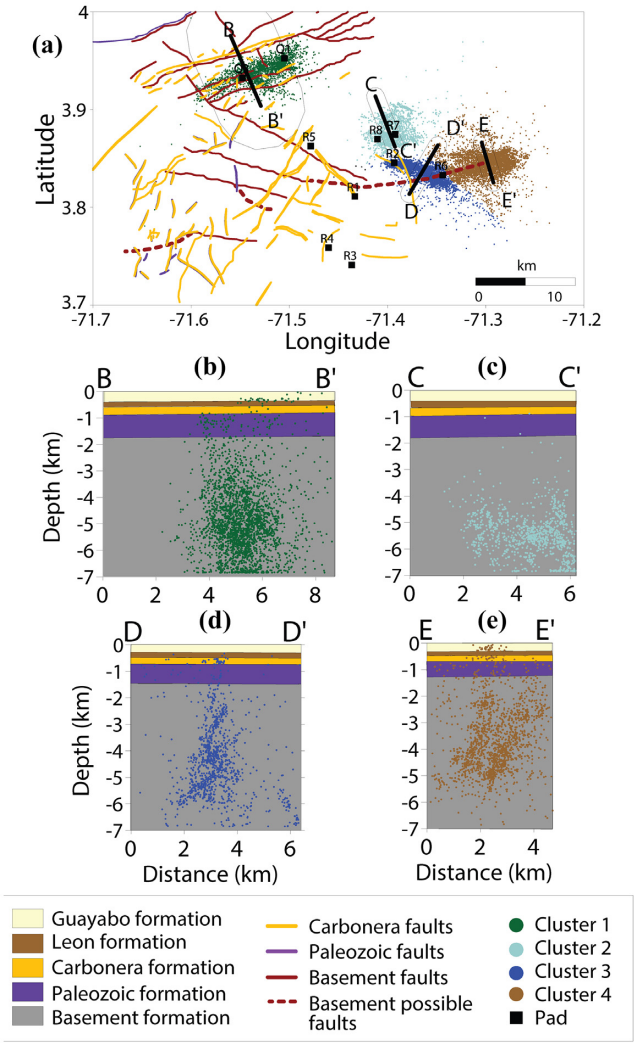

Figure 4. (a) Map of seismicity from the complete catalogue of operator showing clusters 1, 2, 3 and 4, and cross-sections. (b) B–B′ section. (c) C–C′ section. (d) D–D′ section. (e) E–E′ section. Cross-sections are perpendicular sections through different clusters crossed with the geology. B–B′ cross-section has a width of 5 km. The other cross-sections have a width of 1 km. Black squares indicate the location of the pads. Stratigraphic information is only an approximation of the geology of the zone (Pacific Rubiales 2009; Gómez *et al.* 2010; INGRAIN & ANH 2012; Gómez-Alba *et al.* 2015). Note that earthquakes enclosed by faults at Pads Q1 and Q3 (section B–B′) are vertically aligned in the cross-section. Similar behaviour can be seen in sections D–D′ and E–E′. Operator has interpreted vertical faults in the sections B–B′ and D–D′ (unpublished data from the operator). In the section E–E′, the seismic hypocentres suggest two parallel faults. Other sections along the region show vertical faults cutting the formations from Carbonera to the basement formations (Pacific Rubiales Energy 2009; Gomez *et al.* 2010; INGRAIN & ANH 2012).

Quifa extend to a depth of 12 km (Fig. 3b), located between and along four mapped faults trending ENE (Fig. 4a), within 5 km from the injection pads. Further description of the seismicity in this zone can be found in Appendix C and Fig. A2 in Appendix C.

Seismicity began to increase in January and became intense in 2014 April, with 113 events recorded during this month (Appendix A). This seismicity can be divided into three successive swarms that have interevent times ranging from minutes to days, with an average of 6 hr (Fig. 6 and Fig. A2a in Appendix C): swarm I, between the two main faults of the basement at 2–2.5 km WSW of

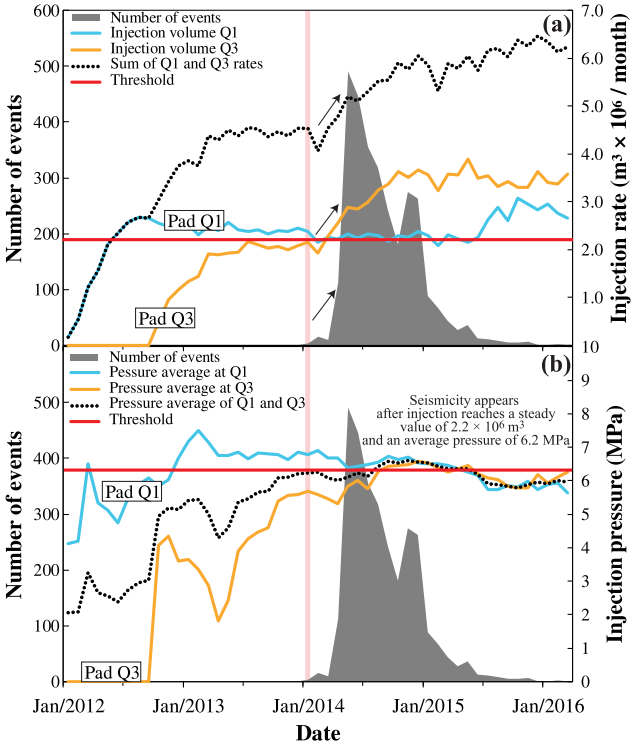

Figure 5. (a) Injection flow rate and (b) pressures compared to the number of events at Quifa field. The first earthquakes appeared when rates at pad Q3 reached for a value of 2.2 × 10^6 m^3 and an average pressure of 6.2 MPa (the period is represented as vertical red band and the threshold of flow rate and pressure is indicated by a red horizontal line) in 2014 January. Note the simultaneous increase in both injection rate at pad Q3 and number of events before 2014 May (indicated by arrows).

pad Q3 in a densely faulted area; swarm II, 1 km E of pad Q3 and 4 km towards SW of pad Q1, many of them of magnitude $M > 3.5$ for swarm II (Apenndix A), perpendicularly to the two main faults of the basement and Carbonera/basement, respectively; swarm III, along a known basement fault, between and perpendicular to the main faults, at about 2.7 km S of pad Q1 and 2.3 km SE of pad Q3. From 2014 May to August, the seismic activity was far more intense with 490 (May), 446 (June), 356 (July) and 318 (August) recorded events, mainly concentrated amid the faults and between the pads Q1 and Q3 (Figs A2b–e in Appendix C). In 2014 September, the 242 recorded earthquakes spread well beyond the northern fault (which strikes ENE, Fig. A2f in Appendix C), after injection volume at injection pad Q3 had sharply increased by 3.2 × 10^6 m^3 in August and by another 3.4 × 10^6 m^3 in September. In 2014 August and October (Figs A2e and f in Appendix C), the earthquakes were close to the injection pads and mainly distributed between the main faults of basement and Carbonera Formations. These earthquakes are located along the main structural features in this zone. After 2014 October, earthquakes were almost exclusively located around injection pad Q1. After 2015 June, seismicity almost stopped (Figs A2g and h in Appendix C).

Beginning in 2014 August, the installation of more stations allowed us to constrain the earthquake depths better (Appendices A and C). The seismicity deepend between 2014 August and 2015 January. From 2014 November to 2015 January, 87 per cent of events originated deeper than 4 km, compared with 72 per cent from 2014 August to October (Fig. A3 in Appendix C). This suggests that increased pore pressure was getting deeper.

Downloaded from https://academic.oup.com/gji/article/223/2/777/5881935 by guest on 07 September 2020

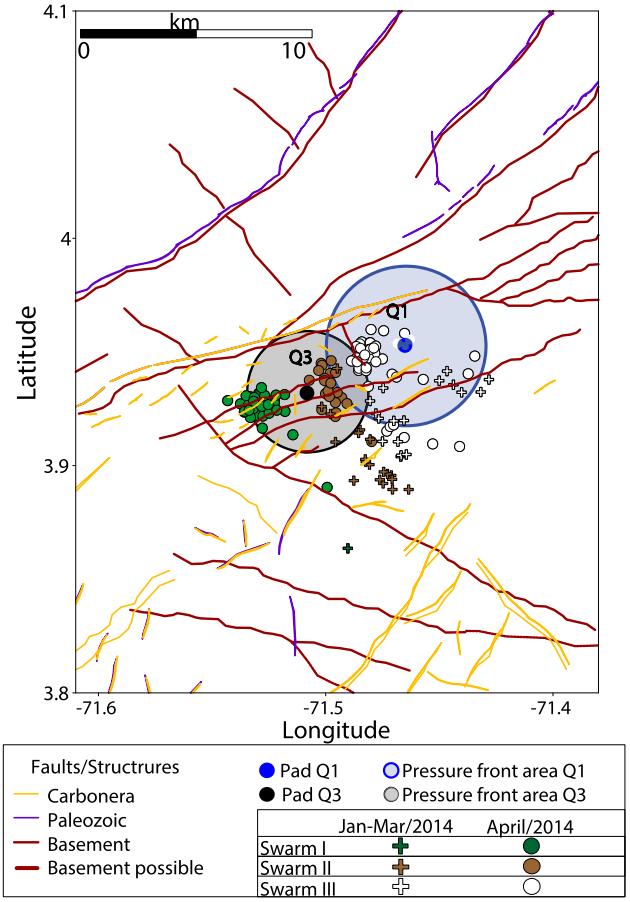

Figure 6. Migration of the pressure disturbance from the beginning of the injection at each pad until 2014 April. Assuming isotropic flow and a hydraulic conductivity of 5.8×10^{-5} m s^{-1}, the front of the increased fluid pressure initiated in 2012 January at pad Q1 has reached a distance of 3.9 km in 2014 April. The overpressure front initiated in 2012 October at Q3 has reached 3 km at the same date.

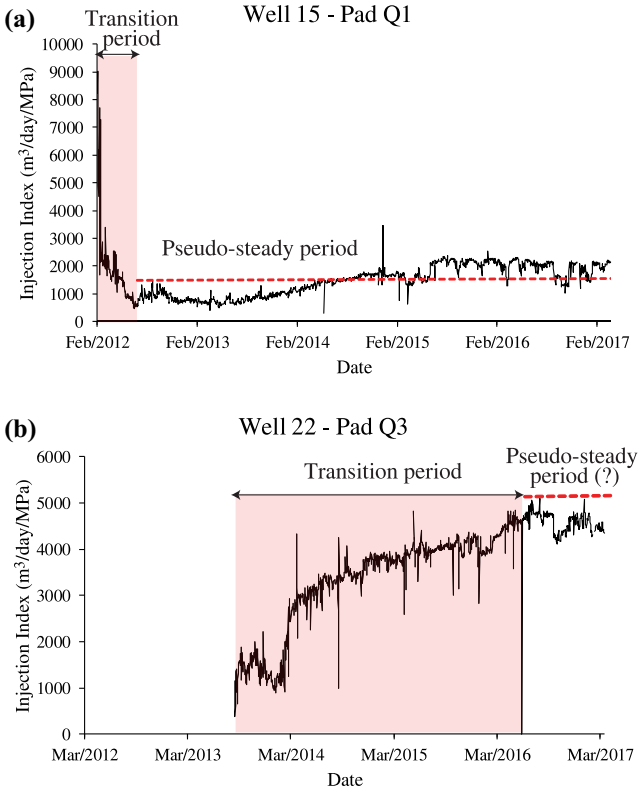

Figure 7. (a) Typical profile of the value of the Injection Index versus time at well 15 of pad Q1 parallel to the fault. The shaded pink area represents the transition period, during which injection flow rate and associated injection pressure vary. (b) Atypical profile of Injection Index versus time for well 22 of pad Q3 perpendicular to the fault.

5.1.2 Injection index, seismicity and hydraulic conductivity

We define that the injection index reaches a stable value when the ratio between the injection flow rate and the associated injection pressure do not vary more than 10 per cent. The injection index calculated for all wells (Table A1) stabilized before the start of the earthquake activity in 2014 January, except for wells 4 and 24, which were drilled in 2013 November and July, respectively (details in Appendix C). They had less time to stabilize than most of the other wells, for which injection started as early as 2012 January. Additionally, well 4 is vertical and its area open to flow is reduced compared to that of horizontal wells.

In Fig. 7(a), we show a typical example of injection index for the well 15 of pad Q1. The injection index behaves similarly for most wells, revealing a transition period between the early times of injection and the stabilization, corresponding to the time required to reach a pseudo-steady-state flow regime. The profile of this transition period is likely to depend on the injection rate, the initial saturation and pressure of the reservoirs and their material properties. The permeability to water of the heavy-oil bearing formation changes until it reaches a stable value. Several wells do not behave as typically, for which an increase of the injection rates does not always correspond to a significant increase of the injection pressure. Fig. 7(b) illustrates an atypical example of the injection index at well 22 at pad Q3, where injection pressure decreases as injection rate increases (Fig. A4 in Appendix C). This profile suggests that the permeability has increased, possibly due to fluid pressure connecting to hydraulically active faults. Once the fluid pressure reaches these faults, they could increase the overall permeability for fluid coming from the injection well. Appearance of the first earthquakes seem to be related to wells with high index values, that are those featuring high permeability (Figs A2 and A5, and details in Appendix C).

Between 2012 October and 2016 March, more than 113 million m^3 of water were injected at the two Quifa injection pads through three different horizons. Permeability along the fault is likely to change as a result of shear dilation (Chin *et al.* 1998); however, with the data on hand, we cannot compute a time dependent permeability. Instead, we estimate the hydraulic conductivity of the medium using the distance reached by the pressure perturbation since the start of the injection until 2014 January, when the first seismic events occurred. The operator provided us with the average permeability of 360 vertical oil wells drilled in adjacent field Rubiales, of similar characteristics, which was 2.5×10^{-12} m^2. Among them, the average permeability of 43 wells drilled over the depth corresponding to the horizontal sections of the injector wells at Quifa field was 2.7×10^{-12} m^2. We use the average of 2.6×10^{-12} m^2 for our calculations (Table 1).

By using the eq. (3) and the input parameters from Table 1, we calculated a hydraulic conductivity K of 5.3×10^{-5} m s^{-1}. Ignoring any temporal changes in permeability, we can estimate the distance

Downloaded from https://academic.oup.com/gji/article/223/2/777/5881935 by guest on 07 September 2020

Table 1. Input and output parameters of hydraulic conductivity.

Parameter/Constant	Symbol	Value	Units	Reference
Permeability	k	2.6×10^{-12}	m^2	Field operator for Quifa
Fluid density	ρ	983.6	$kg\,m^{-3}$	Density of water at 60°C with a salinity of 450 mg l^{-1} (operator): http://www.csgnetwork.com/h2odenscalc.html
Gravity	g	9.81	$m\,s^{-2}$	
Fluid dynamic viscosity	μ	4.67×10^{-4}	kg m−1 s	Viscosity of water at 60°C with a salinity of 450 mg l^{-1} (operator): https://www.hamzasreef.com/Contents/Calculators/WaterProperties.php
Hydraulic conductivity	K	5.3×10^{-5}	$m\,s^{-1}$	Output for Quifa

reached by the pressure perturbation at any given time, particularly the distance at the time of occurrence of the first earthquake (Table 2 and Fig. 6). Seismic swarm I in 2014 April spans a distance of 1.9–2.3 km from Q3. Using a hydraulic conductivity of 5.3×10^{-5} m s^{-1} (4.6 m d^{-1}), such a distance would correspond to the activation of faults by the arrival of a pore pressure perturbation initiated 17 months before at pad Q3, that is in 2012 November (Table A1 in Appendix B, Fig. 6 and Table 2). Considering that injection at pad Q3 started in 2012 October and the uncertainties in hydraulic conductivity due to unknown geological complexities, the occurrence of seismicity in 2012 November is consistent with the hypothesis that injection at Q3 induced swarm I. Likewise, the occurrence of swarm II is consistent with increased pore-pressure perturbations from Q1 and Q3 (Fig. 6) at the time of the seismicity. The fault located 2.7 km ENE from pad Q3 was activated in April 2014, corresponding to the swarm number III. Similar to swarms I and II, much of the seismicity can be explained due to increases in pore-pressure assuming isotropic flow. Some of the seismicity is more distant than our model would predict and the application of eq. (2) does not match the model defined by Shapiro *et al.* 1997 (details in Appendix C).

5.2 Rubiales

5.2.1 Description of seismicity, flow rate and injection pressure

As for the adjacent Quifa field, the rise in seismicity is clearly related to the nearby wastewater injection activities (Figs 8a and b). Injected volumes are extremely high, reaching 5.4×10^5 m^3 of water per day for the eight pads at the end of 2016 July. The first earthquakes recorded close to pad R6 occurred in 2013 July (Appendix A and Fig. A6a in Appendix C) as the volume injected at pad R6 reached 2×10^6 m^3 per month (Fig. 8). Hypocentres developed north of the pad and expanded towards the ENE under the form of an arch, aligned with a possible fault in the basement (Figs A6b–f). Injection rates at pads R1, R3, R4, R5 and R8 never reached the R6 injection rate value (2×10^6 m^3 per month, Fig. 9a) and almost no earthquakes are located nearby. No events were recorded near pads R2 and one might conclude that earthquakes observed in this region are more likely generated by the pressure disturbance migrating from R6 along the existing faults (Fig. A6 and details in Appendix C). Earthquakes near wellpad R2 began up later, long after the start of injection at R2 and after 27 months, a time period consistent with the progression of the pressure disturbance from R6. The first events in the vicinity of pad R7 were recorded in 2013 August (Fig. A6b in the Appendix C) when injection rates reached 1.8×10^6 m^3 per month (Fig. 8b). It appears that seismicity located near pads R7 and R8 largely resulted from injection at pad R7 (Figs A6b and c), when it reached more than 5×10^6 m^3 per month, whereas injection rates at pad R8 peaked at 1.6×10^6 m^3 per month in 2016 May (Fig. 8b). Additionally, seismicity appeared south of cluster 2 (R7 and R8) before the beginning of injection at R8, hence we hypothesize that R7 is contributing to this seismicity.

The average injection rates in Rubiales are about the same as those that triggered seismicity in Quifa, which confirms an injection rate threshold of $\sim 2 \times 10^6$ m^3 per month (Figs 8 and 9a). We deduce that injection at these rates associated to the parameters of our reservoirs generates a pore pressure increase large enough (Fig. 9b) to bring faults to critical conditions. The surface injection pressure associated with the injection rate threshold at the pads source of seismic activity remains below 8.3 MPa (Fig. 9b). However, the change in pore pressure will be significantly lower than this value, since a loss of pressure occurs caused by friction along the wellbore. This pressure loss can reach 10 per cent–15 per cent of the head pressure at these rates.

The average depth of nucleation in the Rubiales field is 4 km (Fig. A7 and details in Appendix C). From 2013 July to December, a majority of events occurred at depth shallower than 4 km. Then, until 2014 December, a majority of the events occurred deeper than 4 km, reaching more than 75 per cent between 2014 January and June. After 2014 July, the earthquakes became progressively shallower and in 2015 March, 52 per cent of them occurred at less than 4 km depth. Then, the evolution was reversed and the percentage of deep events increased again to reach 77 per cent in 2016 July. After 2014 September, the information on the evolution of the depth of hypocentres is more reliable, when the network covered the whole area (Appendix A).

5.2.2 Injection index, seismicity, diffusivity and conductivity

At the pads in this area, injection rate and pressure reach values up to $\sim 5 \times 10^6$ m^3 per month and ∼12 MPa, respectively (Fig. 9). Injection pressure and injection rate are largely anticorrelated: injection volumes are lower at pads injecting at high pressures than those at wells injecting at lower pressures. This low injection index probably results from unfavourable formation parameters and consequently of operational choices (operators typically inject into wells that require the least pressure). We also find an anticorrelation between injection pressure and the occurrence of seismicity near some individual pads. Little seismicity (< 30 events) is recorded within 3 km of the pads R1, R3, R4 and R5 (Appendix A), at which the average injection pressures are higher than 8.3 MPa (Fig. 9b). At pads R6 and R7, injection pressures remain below this threshold and most earthquakes are close to these two pads. The relationship between high seismicity and lower injection pressure may result from hydraulically active faults having higher permeability than the country rock. Thus, for those injection wells where the fluid pressures reach faults, the bulk permeability will be increased by the presence of the fault, hence resulting in lower injection pressures. That pressure perturbations reaching faults could also activate seismicity (examples in Fig. A8 and details in Appendix C). It is also possible that the reactivation of faults would further enhance

Downloaded from https://academic.oup.com/gji/article/223/2/777/5881935 by guest on 07 September 2020

Table 2. Results of maximum distance reached by pressure front at Quifa.

Pad	Injection starting date (dd/mm/yy)	Injection rate reached $\sim 2 \times 10^6$ (m^3/month)	Date chosen for first seismicity (dd/mm/yy)	Maximum distance reached at first events (km)	Maximum distance reached at 10 Apr 2016 (km)	Average injection index ($m^3\ d^{-1}\ MPa^{-1}$)
Q1	04 Jan 2012	May/2012	08 Jan 2014	3.4	6.9	1724
Q3	11 Oct 2012	Mar/2013	08 Jan 2014	2.0	5.8	2305

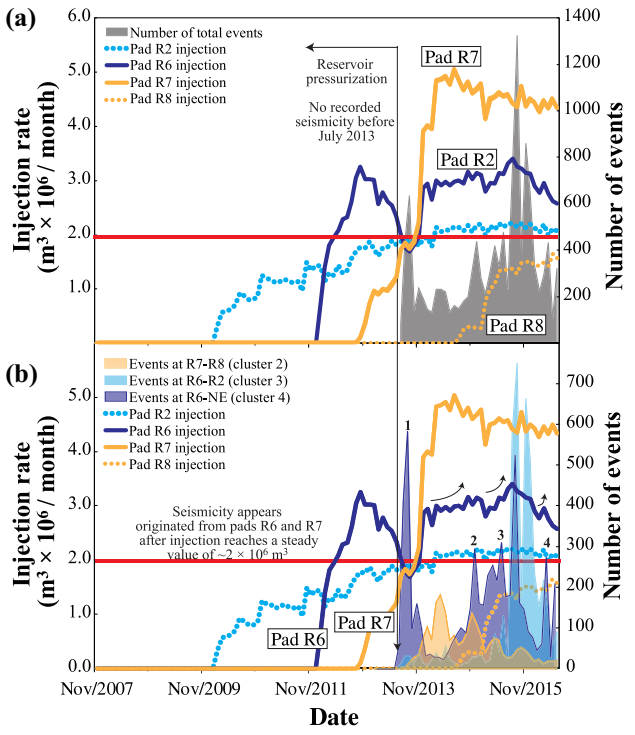

Figure 8. Relationship between injection rate and rise in seismicity for clusters at Rubiales (clusters numbers 2, 3 and 4): (a) total seismic events of $M > 1$ versus injection rate at each pad. (b) Seismicity in each cluster versus injection at each pad. The number of earthquakes in the overlapping area (between clusters 2, 3 and 4) has marked with transparencies and thinner lines compared to the ones for injection rate. It appears that injection, when lower than $\sim 2 \times 10^6$ m^3 per month (horizontal red line) does not generate seismicity for wells R6 and R7 before 2013 July (vertical arrow), with the exception of injection rates of well R6 between 2011 November and 2013 July. Note the peak of seismicity (marked as 1) in 2013 September (marked as 1) at cluster 4 appearing while injection rate for wells R6 decreases, resulting from previous high rate injection. After this date, injection rate for both R6 and R7 remain above 1.7×10^6 m^3 per month and peaks of seismicity (marked as 2, 3 and 4) for this cluster 4 clearly appear after small increases (marked as curved arrows) of injection rates of wells R6.

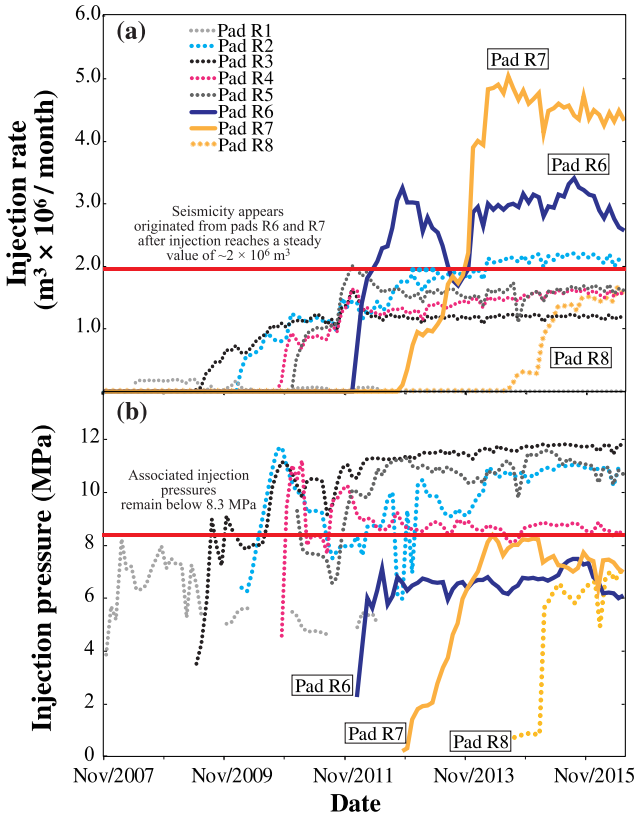

Figure 9. Injection rates and injection pressures for all the pads at Rubiales. (a) Injection rate versus time. Red, horizontal bar represents approximate threshold, above which injection appears to induce seismicity. (b) Injection pressure versus time. Red, horizontal bar represents approximate threshold, above which seismicity does not appear to be induced as most of the seismicity is induced near R6 and R7.

seismicity due to fault zone damage from the slip process. Given variable fault orientations and pathways to faults, the effective permeability seen by each well will be variable and affect the injection pressure accordingly.

Assuming similar fluid/matrix rock parameter values as Quifa (Table 1), we estimate the distances reached by fluid pressure perturbations at different times of interest. They range from a minimum of 3.7 km at pad R8 to 14.5 km at pad R1 in 2016 July (Table 3). The short distance between the multiple pads, the complexity of the faults pattern and the variations in injection rates and pressure at each pad make the surge of seismicity more complex to interpret than that at Quifa, where only two pressure fronts were expanding and interfering (Fig. 6, see details in Section 5.1.2). We then used temporal spreading and applied concept of diffusivity. By using eq. (2), we determined the best model to estimate the scalar diffusivity for clusters 2, 3 and 4 at Rubiales. We show an example in Fig. 10. We obtained scalar diffusivities in the order of 2.0×10^{-2}–9.3×10^{-2} $m^2\ s^{-1}$ (details in Appendix C). The average scalar conductivity of 3.4×10^{-5} $m\ s^{-1}$ and injection index values of 1300 $m^3\ d^{-1}\ MPa^{-1}$ are in the same order of magnitude as the ones calculated for Quifa, suggesting that hydraulic properties of Quifa and Rubiales are similar (Tables 1 and 2, Figs A5 and A9 and details in Appendix C).

5.3 Local stress field

Following Aki &Richards (1980), focal mechanisms were classified as strike-slip, normal and reverse faulting based upon the rake angle. The focal mechanisms reveal that faulting is predominantly

Downloaded from https://academic.oup.com/gji/article/223/2/777/5881935 by guest on 07 September 2020

Table 3. Results of maximum distance reached by pressure front at Rubiales.

Pad	Injection starting date (dd/mm/yy)	Injection rate reached $\sim 2 \times 10^6$ (m^3 per month)	Date chosen for first seismicity (dd/mm/yy)	Maximum distance reached at first events (km)	Maximum distance reached at Jul/2016 (km)	Average injection index ($m^3\ d^{-1}\ MPa^{-1}$)
R1	23 Nov 2007	–	–	–	14.5	357
R2	11 Feb 2010	Sep/2012	01 Apr 2014	6.5	10.8	1688
R3	15 May 2009	Jan/2017	–	–	12.0	1024
R4	19 Oct 2010	–	–	–	9.6	1831
R5	03 Jan 2011	Dec/2011	–	–	9.3	749
R6	02 Jan 2012	Mar/2012	01 Jul 2013	2.5	7.6	1126
R7	22 Oct 2012	Jul/2013	01 Jul 2013	1.2	6.3	2662
R8	15 May 2014	–	–	–	3.7	940

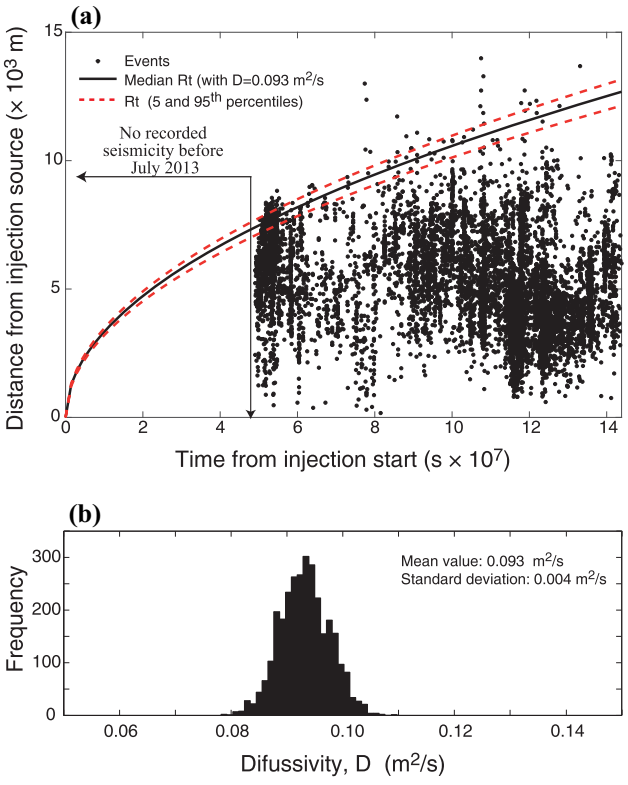

Figure 10. (a) Example of an R-T (distance–time) plot for the seismicity recorded from pad R6 toward the NE, since the beginning of injection at pad R6 in 2012 January 2. The continuous black line shows the 'triggering front' boundary estimated considering a scalar diffusivity of the order of 9.3×10^{-2} $m^2\ s^{-1}$; the discontinuous lines represent the 5th and the 95th percentiles of the triggering front according to the uncertainties in the estimated value of diffusivity. (b) Histogram of scalar diffusivity samples obtained using the MCMC method implemented for the parameter value inference (mean value 9.3×10^{-2} $m^2\ s^{-1}$, standard deviation 0.004 $m^2\ s^{-1}$).

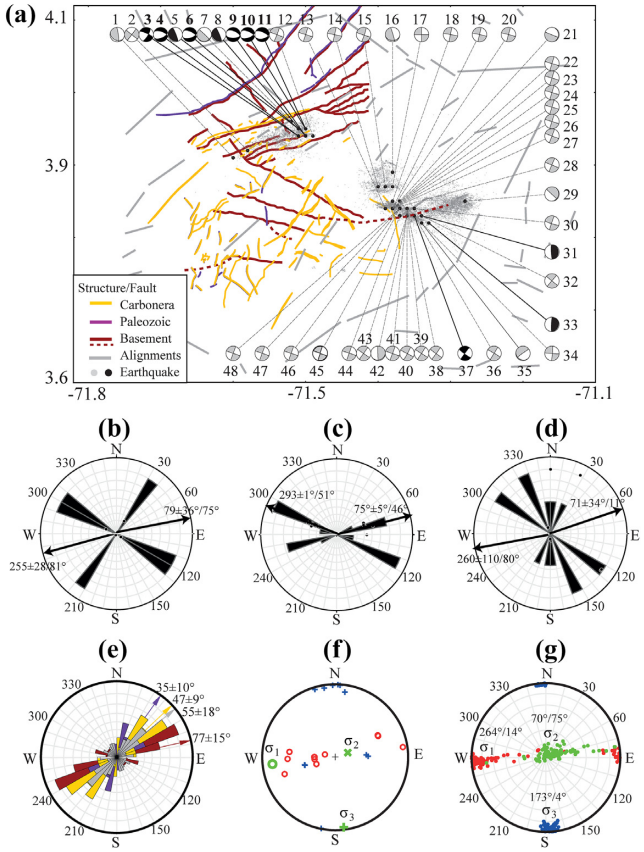

Figure 11. Stress field derived from focal mechanisms and relationship between fault detections given by the operator and focal mechanisms: (a) focal mechanisms with filled black quadrants are high-quality solutions (STDR $\geq$ 0.4) and they were taken into account to produce the figures (b)–(d), (f) and (g); while focal mechanisms with filled gray quadrants are low-quality solutions (STDR $<$ 0.4). (b)–(d) Rose diagram with strike and dip angles for each faulting style determined through focal mechanisms shown in (a) strike-slip, normal and reverse regimes, respectively. The values at the tip of each rose represent the mean value of azimuth/plunge for each regime and their two nodal planes. (e) Rose diagram with strike angles of the faults detected through seismic interpretation performed by operator in the different geological formations. (f) The direction of maximum compression (red circles) and minimum compression (blue crosses) are shown for each earthquake. The preferred principal stress directions are shown by green symbols. (g) Principal stress axes and their uncertainty according to Jack-knife test of stability of the solutions. Clusters of same coloured symbols show the confidence zones of maximum σ_1 (red), medium σ_2 (green) and minimum σ_3 (blue) stress axes orientations. The values of the azimuth/plunge for stress axes are shown.

strike-slip in the Rubiales field, while being mostly normal at Quifa field (Fig. 11a). The orientation of some of the fault planes as determined from the focal mechanisms are well correlated with both the orientation of the mapped faults and the planes outlined by the event locations (Fig. 11a). The seismicity was also predominantly in areas with a higher density of mapped faults (unpublished data shared by the operator). The strike-slip mechanisms, normal and reverse for mechanisms with STDR $\geq$ 0.4 give nodal planes striking to the ENE and WSW, WNW and ENE, and ENE and WSW,

Downloaded from https://academic.oup.com/gji/article/223/2/777/5881935 by guest on 07 September 2020

respectively, with one of the nodal planes suggesting steeply dipping structures for the strike-slip and reverse mechanisms (Figs 11b and d, and details in Appendix C). Faults mapped by the operator and alignments of structures show similar azimuths as the strike-slip mechanisms, normal and reverse focal mechanisms (compare Figs 11b–d with Fig 11e, details in Appendix C). Thus, the fault planes derived from source mechanism indicate that stresses have the same trends than that of the mapped faults. The variation of fault trends along the stratigraphic units indicates different deformation events that have affected the area. Most of the plunges determined from our source mechanisms indicate vertical faults (Figs 11b and d), in agreement with the fault interpretation given by the operator (INGRAIN & ANH 2012; unpublished data shared by the operator) and the almost vertical distribution of earthquakes (Figs 4b and e).

We inverted the local stress field using the focal mechanisms of the earthquakes (Table A3 in Appendix B) and the results are summarized in Table A4 in Appendix B (Figs 11f and g). We compute a maximum compressional stress (σ_1) that is near horizontal (plunge 14°), striking at 264°. This is consistent with the orientation of SH_{max} as determined with borehole breakout data (240°–250°; unpublished data shared by the operator). The intermediate principal stress (σ_2) is near vertical (plunge 75°), implying that regional stress field is predominantly strike-slip. The three stress axes σ_1, σ_2 and σ_3 are stable when randomly perturbing the input focal mechanism within their expected uncertainties and/or when constraining the friction coefficient at various values. The shape ratio is 0.28, which is consistent with this being a predominantly strike-slip system.

6 DISCUSSION

6.1 Injection rate triggering threshold

We confirmed a strong correlation between injection rate and seismicity, after the injection rates reach a threshold of $\sim 2 \times 10^6$ m^3 per month. Relative to other areas of wastewater injection, the volumes disposed at Quifa and Rubiales fields (0.6×10^7 and 1.5×10^7 m^3 per month in 2016 April, respectively) are high. They are of the same order of magnitude as the volumes of wastewater injected in the Arbuckle group in Oklahoma (1.4×10^7 m^3 per month at their peak of 2015), where the effect of injection on seismicity in Oklahoma is well documented (e.g. Walsh & Zoback 2015; Langenbruch & Zoback 2016). These authors respectively found that very little induced seismicity occurred before injection rates had exceeded 1.2×10^6 m^3 per month and confirmed that it started after a threshold of 3.6×10^6 m^3 per month had been reached. For similar injected volumes, our study area covers $\sim 3 \times 10^3$ km^2, while the Oklahoma Area of Interest is two orders of magnitude larger ($\sim 2 \times 10^5$ km^2). Despite the injection being spread across a much larger region, Oklahoma has had much more and larger seismicity (M_{max} 5.8) than what has been observed in our study area. The difference in the seismic response is likely due to the simultaneous production and injection of almost similar volumes of water into the same formation at Quifa and Rubiales, while the injection in Oklahoma is into a hydrologic group that is largely undisturbed by oil and gas extraction. The oil production in our study area reduces the overall pressure increase caused by injection, thus reducing the likelihood of inducing earthquakes.

6.2 Fluid injection, stress field and spatial distribution of seismicity

Between 1989 and 2009, more than 40 million of barrels of oil were produced from the Quifa and Rubiales fields, and the average reservoir pressure remained nearly constant at its initial value around 7.6 MPa with the active aquifer replacing the volume of oil (Villegas *et al.* 1994). Formation water was produced in increasingly larger quantities through hundreds of wells and reinjected using a few dedicated wells. This injection of wastewater resulted in an increase of the prevailing reservoir pressure, raising it to 8 MPa at the points of injection.

There is almost no record of felt seismicity in this area before the first seismic swarms occurred in 2013 and localized within 6 km from the injection pads in Quifa and Rubiales along identified faults (Figs 3, 4, 7, 11 and Figs A2 and A6). The first activated faults (2013 July) are mainly located in the basement, close to the Rubiales field, and oriented ENE (Appendix A and Fig. A6a in Appendix C). The seismicity swarms were then concentrated near the Quifa injection pads, as well as near the R6, R7 and R2 pads at Rubiales. The cause of this seismicity can be explained by different concomitant factors as (i) the increased fluid pressure, ranging between 6–8 MPa (Figs 5b and 9b); (ii) a higher density of faults, most of which are well-oriented for failure in the local stress field (Figs 3a and 4a); and (iii) the high injection rates in the wells located in these areas ($\sim 2 \times 10^6$ m^3 per month, Figs 5a, 8 and 9a). Therefore, fault density, preferable fault orientation, and proximity to failure are probably the main geologic factors controlling the occurrence of seismicity.

6.3 Correlation between seismicity and injection rates

A unique feature of this earthquake sequence is that subsequent to the increase in seismicity that lasted for approximately 3 yr, earthquake rates since have declined, despite the fact that injection rates have remained high at both Quifa and Rubiales. In contrast, seismicity rates declined months after the injection rate was reduced in Oklahoma (Langenbruch & Zoback 2016). The significant drop in the number of earthquakes in the vicinity of the injection points may be due to two reasons: (i) most of the available tectonic stress has been released through seismicity, at a rate faster than the tectonic reloading, (ii) the activation of faults may have changed some characteristics of the medium, particularly its permeability, and the associated pressure was therefore no longer rising.

As the pressure front continued to expand with the ongoing injection, no new earthquakes seem to occur beyond the areas over which the activity is mainly concentrated. The absence of more distant seismicity could arise from a number of reasons including: (i) the pore pressure has not exceeded a critical value required for inducing slip in optimally oriented faults located at the distance reached by the fluid pressure perturbation, (ii) there are not well-oriented faults at the distances to which the fluid-pressure has reached and (iii) there may not be fluid pathways to reach the areas of well-oriented faults.

We cannot pinpoint which specific wells are causing these earthquakes because wastewater is injected into different geological formations through 70 mostly horizontal wells. Differing injection start times, injection rates and pressures all make a one-to-one connection very difficult. Instead, we examine the combined effect and observe that the pressure perturbation and the subsequent seismic activity are mainly related to the wastewater injection rate.

At rates or pressures insufficient to activate a fault adequately oriented, the pressure perturbation may ‘cross’ faults without generating seismicity. The pressure disturbance generated at pad Q1

Downloaded from https://academic.oup.com/gji/article/223/2/777/5881935 by guest on 07 September 2020

crossed the fault located WSW (between pads Q1 and Q3) without generating seismicity, but this fault was activated in 2014 April when it was influenced by the additional pressure disturbance generated at pad Q3 (Fig. 6). This observation is in agreement with the work presented by Mukuhira *et al.* (2016), who reported how only some parts of a fault enter the critical state during injection, while a large part of the fault can be destabilized during shut-in due to uniformization of pore pressure distribution. Considering the large quantity of injected water (over 800 million m^3) and the duration of the injection (up to 7 yr for Rubiales), the pressure disturbance at Rubiales and Quifa fields probably reached distances larger than the localization of the most distant recorded earthquakes.

Several experimental and case studies consider seismicity induced by linear and nonlinear fluid−rock interaction (e.g. Shapiro 2015), and most models consider a single or a few injection wells. Statistical approaches to forecast seismicity rates or to estimate the probability of occurrence of large magnitude events are mainly based on the current status of induced seismicity (e.g. Bachmann *et al.* 2011; Mena *et al.* 2013; Garcia-Aristizabal 2018; Petersen *et al.* 2018) and often do not consider any information about the geology or injection operations in the area. Others have used physical models to consider the probability of a pressure disturbance to activate faults randomly distributed in the surrounding rocks (e.g. Shapiro 2015; Norbeck & Rubinstein 2018), instead of the actual distribution of faults. We have compiled and summarized up-to-date structural and geomechanical information for this zone; the direction of the maximum compressive stress obtained through focal mechanisms (Fig. 11g) is in agreement with *in situ* measurements documented by field operators (unpublished data shared by the operator). The 3-D seismic surveys provided by the operator indicate that faults detected in the Carbonera formations are parallel to faults in the palaeozoic and basement (Figs 11a and e); this suggests a probable hydraulic connection between the Carbonera and basement, as wastewater is mostly injected in Carbonera. With the knowledge of several mapped faults and the trends in seismicity (Figs 11a–e), we think that fluid migrated from the pads through these existing faults and caused those earthquakes. We can see this particularly clear in the Quifa area, for which a large quantity of data has been provided by the field operator (Figs 3, 4, 6 and 11a).

6.4 Spatial migration of seismicity

As the pressure disturbance font expands, it will 'cross' new faults whose characteristics (orientation and stress) are hydraulically active and favourable to slip. Under the same geomechanical conditions, it is expected that faults located at greater distances from an injection pad will usually be activated later respect to the closer ones. Seismicity at the N, S and NW of cluster 2, occurred between pads R7 and R8, where seismic trends in the direction WNW and NNE start to appear in 2014 April (Appendix A and Fig. A6f in Appendix C). However, it is also possible that faults located near the injection wells can be activated at later times, resulting from (i) anisotropic flow regimes, (ii) faults not having reached their failure criteria or being poorly oriented under the current stress regime and (iii) stress-triggering effects associated to stress perturbations caused by previous earthquakes. Such mechanisms may explain why swarms are not exclusively expanding from the injection pads outward, and why earthquakes seem to move 'back-and-forth' (e.g. the seismicity observed from pad R6 to the NE or between pads Q1 and Q3). As injection continues, additional pressure may activate faults that were not affected by lower pressure. Some hypocentres reach 12 km depth (Fig 3b) and are distributed along known, near-vertical faults, providing a possible pathway to connect the basal sands with the basement (Figs 4b–e).

7 CONCLUSIONS

We have shown that the injection of a large amount of wastewater resulted in the occurrence of seismicity in two contiguous oil fields (Quifa and Rubiales) near Puerto Gaitán, Colombia. After a period of 3 yr, the earthquake rate significantly decreased without reduction of the injection rates.

i) The increased pore pressure on faults near injection wells reactivated these faults and much of the induced seismicity lies on or near them. Several mapped faults and seismic trends coincide with focal mechanism planes and these faults are likely the pathways of the fluid from the disposal formation into the basement. In some clusters, the spatio-temporal distribution of earthquakes shows vertical alignment and deepening, indicating that the pore pressure perturbation follows these paths.

ii) By visual inspection, we find a strong correlation between the time history of injection and seismicity. Specifically, we find that there is an apparent threshold injection rate, identified to be approximately 2×10^6 m^3 per month, above which injection rates must rise for injection to induce earthquakes. This rate is associated to an injection surface pressure lower than 8.3 MPa, able to sustain a pressure disturbance large enough to activate faults.

iii) The increase of the bulk permeability resulting from the presence of hydraulically active faults whose permeability is higher than that of the country rock is evidenced by the unexpected association of high injection rates and low injection pressure, itself resulting in an anticorrelation of injection rates and seismicity.

iv) Despite the uncertainties due to unknown geological complexities, a value for the hydraulic conductivity of 5.3×10^{-5} m s^{-1} fits the relationship between the elapsed time since injection started and the distance reached by the pore pressure perturbation. As of 2016 July, injection is likely affecting the reservoir pressure at distances at which no seismicity is occurring, suggesting that the perturbation amplitude is no longer sufficient or that stress conditions and (or) orientation are no longer met for the faults to be activated.

v) The decline in seismicity observed at the Quifa and Rubiales fields despite the unabated injection reveals information about the regional stress. Specifically, we conclude that these earthquakes have released most of the tectonic stress, such that there is not enough stress available to be relieved in additional earthquakes. Given the short period of time and modest tectonic loading rate, faults in the area have not re-loaded enough to produce earthquakes.

vi) The water cut having reached over 95 per cent, the quantity of injected water is unlikely to increase significantly in the future. Seismic activity may resume, if injection is sustained long enough to build up the pressure disturbance over large distances.

ACKNOWLEDGEMENTS

This work was supported by the Servicio Geológico Colombiano (SGC) and the FAPA project (Fondo de Apoyo para Profesores Asistentes) No. INV-2019-63-1702 from the Universidad de los Andes, Colombia. All the seismic and industrial data used in this work were made available by the SGC (https://www.sgc.gov.co/); it includes the seismic data produced by SGC, as well as the seismic and industrial data obtained by inter-institutional agreements with the field operator. We are deeply grateful to Pacific Rubiales Energy

Downloaded from https://academic.oup.com/gji/article/223/2/777/5881935 by guest on 07 September 2020

for allowing us to publish their field and interpretation data, and to Wilson Parra and Diego Morales for numerous fruitful discussions. We thank Nelson Perez and Nehify Pablos, from SGC, for their contribution to the determination of focal mechanisms and faults parameters, respectively. We recognize the contribution from Jose Calderón, Pedro Galindo and Laura Pérez from Ecopetrol for their valuable comments. We thank Jaime Romero and his team from SGC for sharing the data set of alignments, John Makario Londoño from SGC for sharing his codes for inversion of magnitude and his knowledge of the Velest software. We also thank Estella Ordoñez from SGC for performing the data picking process. Reviews by Dan McNamara, Art McGarr, and Elizabeth Cochran on an early version of this work significantly improved this manuscript. We thank the Editor and the two anonymous reviewers for their suggestions and helpful comments that improved this manuscript. Any use of trade, firm, or product names is for descriptive purposes only and does not imply endorsement by the U.S. Government.

REFERENCES

Aki, K. & Richards, P.G., 1980. *Quantitative Seismology: Theory and Methods,* 2nd edn, Vol. **I,** W.H. Freeman and Co, San Francisco, 557pp.

Bachmann, C.E., Wiemer, S., Woessner, J. & Hainzl, S., 2011. Statistical analysis of the induced Basel 2006 earthquake sequence: introducing a probability-based monitoring approach for Enhanced Geothermal Systems, *Geophys. J. Int.,* **186**(2), 793–807.

Bailey, I.W., Ben-Zion, Y., Becker, T.W. & Holschneider, M., 2010. Quantifying focal mechanism heterogeneity for fault zones in central and southern California, *Geophys. J. Int.,* **183**(1), 433–450.

Barbour, A.J., Norbeck, J.H. & Rubinstein, J.L., 2017. The effects of varying injection rates in Osage County, Oklahoma, on the 2016 Mw 5.8 Pawnee earthquake, *Seismol. Res. Lett.,* **88**(4), 1040–1053.

Biot, M.A., 1956. Theory of propagation of elastic waves in a fluid-saturated porous solid. I. Low-frequency range. *J. acoust. Soc. Am.,* **28**(2), 168–178.

Chin, L.Y., Raghavan, R. & Thomas, L.K., 1998. Fully-coupled geomechanics and fluid-flow analysis of wells with stress-dependent permeability, in *SPE International Oil and Gas Conference and Exhibition in China,* Society of Petroleum Engineers, 32–45.

Cooper, M.A. *et al.*, 1995. Basin development and tectonic history of the Llanos Basin, Eastern Cordillera, and middle Magdalena Valley, Colombia, *AAPG Bull.,* **79**(10), 1421–1442.

Dasilva, A., Gomez, Y., Villa, M.A., Yoris, F. & Morales, D., 2013. Oil distribution in the Carbonera formation, Arenas Basales Unit. A case study in the Quifa and Rubiales Fields, Eastern Llanos Basin, Colombia, in *Adapted from Extended Abstract Prepared for a Poster Presentation at AAPG International Conference and Exhibition,* Cartagena, Colombia, AAPG Datapages Inc., Search and Discovery, 1–10.

Ellsworth, W.L., 2013. Injection-induced earthquakes. *Science,* **341**(6142),.

Evans, D., 1966. The Denver Area earthquakes and the rocky mountain arsenal disposal well, *Mt. Geol.,* **3**(1), 23–36.

Garcia-Aristizabal, A., 2018. Modelling fluid-induced seismicity rates associated with fluid injections: examples related to fracture stimulations in geothermal areas. *Geophys. J. Int.,* **215**(1), 471–493.

Garcia-Aristizabal, A., Caciagli, M. & Selva, J., 2016. Considering uncertainties in the determination of earthquake source parameters from seismic spectra. *Geophys. J. Int.,* **207**(2), 691–701.

Goebel, T.H. & Brodsky, E., 2018. The spatial footprint of injection wells in a global compilation of induced earthquake sequences. *Science,* **361**(6405), 899–904,.

Gómez-Alba, S., Fajardo-Zarate, C. & Vargas, C., 2015. Stress field estimation based on focal mechanisms and back projected imaging in the Eastern Llanos Basin (Colombia), *J. South Amer. Earth Sci.,* **71,** 320–332.

Gómez-Alba, S., Vargas, C. & Zang, A., 2020. Evidencing the relationship between injected volume of water and maximum expected magnitude during the Puerto Gaitán (Colombia) earthquake sequence from 2013 to 2015, *Geophys. J. Int.,* **220,** 335–344.

Gómez, Y., Yoris, F., Rodriguez, J., Portillo, F. & Araujo, Y., 2010. Aspectos hidrodinámicos, estructurales y estratigráficos del Campo Rubiales, Colombia, *Rev. Geo Petróleo ACGGP,* **9,** 4–10.

Healy, J., Rubey, W., Griggs, D. & Raleigh, C., 1968. The Denver Earthquakes, *Science,* **161**(3848), 1301–1310.

INGRAIN &AANH, 2012. CUENCA LLANOS ORIENTALES Integración Geológica de la Digitalización y Análisis de Núcleos, *Public Report of the Agencia Nacional de Hidrocarburos (ANH) of Colombia,* Colombia, 209, http://www.anh.gov.co/Informacion-Geologica-y-Geofisica/Tesis/5.%20Informe%20Final%20Llanos.pdf (last accessed: July 2020).

Keranen, K.M., Weingarten, M., Abers, G.A., Bekins, B.A. & Ge, S., 2014. Sharp increase in central Oklahoma seismicity since 2008 induced by massive wastewater injection, *Science,* **345**(6195), 448–451.

Langenbruch, C. & Zoback, M.D., 2016. How will induced seismicity in Oklahoma respond to decreased saltwater injection rates?, *Science Advances,* **2**(11), 1–9,.

Lei, X.L, Yu, G., Ma, S., Wen, X. & Wang, Q., 2008. Earthquakes induced by water injection at 3 km depth within the Rongchang gas field, Chongqing, China, *J. geophys. Res.,* **113**(B10310), 1–12.

Leptokaropoulos, K., Karakostas, V., Papadimitriou, E., Adamaki, A., Tan, O. & Inan, S., 2013. A homogeneous earthquake catalog for Western Turkey and magnitude of completeness determination., *Bull. seism. Soc. Am.,* **103**(5), 2739–2751.

MacQueen, J., 1967, Some methods for classification and analysis of multivariate observations. In Cam, L. Le & Neyman, J.eds, *Proc. Berkeley Symp. on Mathematical Statistics and Probability* , **Vol. 1,** University of California Press, p. 281–297.

Mena, B., Wiemer, S. & Bachmann, C., 2013. Building robust models to forecast the induced seismicity related to geothermal reservoir enhancement, *Bull. seism. Soc. Am.,* **103**(1), 383–393.

Michael, A.J., 1987. Use of focal mechanisms to determine stress: a control study, *J. geophys. Res.,* **92**(B1), 357–368.

Mukuhira, Y., Dinske, C., Asanuma, H., Ito, T. & Häring, M.O., 2016. Pore pressure behavior at the shut-in phase and causality of large induced seismicity at Basel, Switzerland, *J. geophys. Res. Solid Earth,* **122** (1), 411–435.

Nguyen, L.M., Lin, T.L., Wu, Y.M., Huang, B.S., Chang, C.H., Huang, W.G., Le, S.T. & Dinh, V.T., 2011. The first M_L scale for North of Vietnam, *J. Asian Earth Sci.,* **40**(1), 279–286.

Norbeck, J.H. & Rubinstein, J.L., 2018. Hydromechanical earthquake nucleation model forecasts onset, peak, and falling rates of induced seismicity in Oklahoma and Kansas, *Geophys. Res. Lett.,* **45**(7), 2963–2975.

Orlecka-Sikora, B. *et al.*, 2020. An open data infrastructure for the study of anthropogenic hazards linked to georesource exploitation, *Sci. Data,* **7**(89), 1–16.

Pacific Rubiales Energy, Meta Petroleum Ltd., Pacific Rubiales Energy y ECOPETROL, Contrato de Asociación Rubiales-Pirirí, 2009. Estudio integrado de yacimientos campo Rubiales, *Reporte del modelo estructural,* Bogota, D.C., Colombia, 1–40.

Petersen, M.D. *et al.*, 2018. 2018 one-year seismic hazard forecast for the Central and Eastern United States from induced and natural earthquakes, *Seismol. Res. Lett.,* **89**(3), 1049–1061.

Raleigh, C.B., Healy, J.H. & Bredehoeft, J.D., 1976. An experiment in earthquake control at Rangely, Colorado, *Science,* **191**(4233), 1230–1237.

Reasenberg, P.A. & Oppenheimer, D., 1985. FPFIT, FPPLOT and FPPAGE: FORTRAN computer programs for calculating and displaying earthquake fault-plane solutions, *Open-File Rep, U.S. Geol. Surv.,* 85–739.

Rice, J.R. & Cleary, M.P., 1976. Some basic stress diffusion solutions for fluid-saturated elastic porous media with compressible constituents, *Rev. Geophys. Space Phys.,* **14**(2), 227–241.

Rubinstein, J.L., Ellsworth, W.L. & Dougherty, S.L., 2018. The 2013–2016 induced earthquakes in Harper and Sumner Counties, Southern Kansas, *Bull. seism. Soc. Am.,* **108**(2), 674–689.

Rubinstein, J.L., Ellsworth, W.L., McGarr, A. & Benz, H.M., 2014. The 2001–present induced earthquake sequence in the Raton basin of northern New Mexico and southern Colorado, *Bull. seism. Soc. Am.,* **104**(5), 2162–2181.

Downloaded from https://academic.oup.com/gji/article/223/2/777/5881935 by guest on 07 September 2020

Schwartz, F.W. & Zhang, H., 2002. *Groundwater,* John Wiley & Sons Inc., New York, 592pp.
Shapiro, S.A., 2015. *Fluid-Induced Seismicity,* Cambridge University Press, 289pp.
Shapiro, S.A., Huenges, E. & Borm, G., 1997. Estimating the crust permeability from fluid-injection-induced seismic emissions at the KTB site, *Geophys. J. Int.,* **131**(2), F15–F18.
Shapiro, S.A., Rothert, E., Rath, V. & Rindschwentner, J. 2002. Characterization of fluid transport properties of reservoirs using induced microseismicity, *Geophysics,* **67**(10), 212–220.
Stabile, T.A., Giocoli, A., Perrone, A., Piscitelli, S. & Lapenna, V., 2014. Fluid injection induced seismicity reveals a NE dipping fault in the southeastern sector of the High Agri Valley (southern Italy), *Geophys. Res. Lett.,* **41**(16), 5847–5854.
Van Der Kamp, G. & Gale, J.E., 1983, Theory of earth tide and barometric effects in porous formations with compressible grains, *Water Resour. Res.,* **19**(2), 538–544.
Vavryčuk, V., 2014. Iterative joint inversion for stress and fault orientations from focal mechanisms, *Geophys. J. Int.,* **199**(1), 69–77.
Villegas, M.E., Bachu, S., Ramon, J.C. & Underschultz, J.R., 1994, Flow of formation waters in the Cretaceous-Miocene succession of the Llanos Basin, Colombia, *AAPG Bull.,* **78**(12), 1843–1862.
Walsh, F.R.I. & Zoback, M.D., 2015. Oklahoma's recent earthquakes and saltwater disposal, *Sci. Adv.,* **1**(5), 1–9.
Wiemer, S. & Wyss, M., 2000. Minimum magnitude of completeness in earthquake catalogs: examples from Alaska, the Western United States, and Japan, *Bull. seism. Soc. Am.,* **90**(4), 859–869.
Yeck, W.L., Weingarten, M., Benz, H.M., McNamara, D.E., Bergman, E.A., Herrmann, R.B., Rubinstein, J.L. & Earle, P.S., 2016. Far-field pressurization likely caused one of the largest injection induced earthquakes by reactivating a large preexisting basement fault structure, *Geophys. Res. Lett.,* **43**(19), 10198–110207.

SUPPORTING INFORMATION

Supplementary data are available at *GJI* online.

MOVIE 1. Evolution of earthquakes locations in relation with pads, seismic stations, acquisition polygons and faults. Yellow stars indicate earthquakes with re-calculated magnitudes (See Section 4.1 of the main text) yielding M > 3.5.
Table A1. List of starting dates of injection and Injection Index at specific wells per pad.
Table A2. Station correction for magnitude calculation.
Table A3. Complete list of earthquake focal mechanisms solutions including the parameters of strike, dip and rake for the two nodal planes solutions[(1),(2)], STDR (station distribution ratio), the fraction of polarity misfit (0 = perfect fit, 1 = perfect misfit) according to Reasenberg & Oppenheimer (1985) and local magnitude scale M_L. The events that were used to calculate the stress tensor are enhanced in bold.
Table A4. Parameters of the principal stress axes based on the inversion from aftershocks whose STDR $\geq$ 0.4.
Figure A1. (a) Wadati plot for velocity model (red line is the regression fit) and comparison of earthquake locations, and magnitudes derived from our model and that of the operator, and results of magnitude inversion to determine the magnitude formula in the Puerto Gaitán region: (b) origin time difference. (c) Depth difference. (d) Epicentral difference. (e) Magnitude of completeness (M_c) for operator catalogue based on maximum-likelihood solution. (f) Comparison between the calculated log A_0 by distance-correction function as $-\log A_0 = 1.02\log(r/17) + 0.022(r - 17) + 2$ (see details in Nguyen *et al.* 2011), and 5604 observed peak Wood–Anderson amplitudes of 697 earthquakes from 20 stations. (g) Comparison of the magnitudes of earthquakes resulting of the new equation and that used by operator. (h) Comparison of the magnitudes of earthquakes resulting of the new equation and that used by SGC before getting this new formula. Blue line emphasizes the relation 1:1 and red line is the regression fit.
Figure A2. Earthquakes location and migration at Quifa at different periods: (a) 2014 January–April, (b) 2014 May, (c) 2014 June, (d) 2014 July, (e) 2014 August, (f) 2014 September–December, (g) 2015 January–May, (h) 2015 June to 2016 April and (i) 2014 January to 2016 April. (a) The magenta and grey dots are hypocentres from 2014 January–March and April, respectively; red lines spreading from disposals wells represent the horizontal section, surveys. Some wells at pad Q1 and Q3 are numbered and referenced in the text, and (i) magenta dots are hypocentres between 2014 January and March, blue dots are hypocentres between 2014 April and December, green dots between 2015 January and May, brown dots between 2015 June and 2016 April. Note that events are increasingly confined between pads Q1 and Q3 over time.
Figure A3. Earthquakes depth evolution at Quifa: from 2014 January to April, 60 per cent of earthquakes initially nucleated at less than 4 km. Then, the depth of origin was deeper than 4 km: 75 per cent from 2014 May to July, 72 per cent from 2014 August to October, 87 per cent from 2014 November to 2015 January.
Figure A4. Injection rate and injection pressure as a function of time. The injection rate increases while the injection pressure decreases.
Figure A5. Injection index at: (a) C1 Sandstones and (b) Basal Sandstones. Too few wells have been drilled in sand C1 to present a representative correlation. Blue dots on (a) represent wells drilled in Basales at Pad Q1. All wells of Pad Q3 (red dots) have been drilled in the Basal sandstone formation. Wells numbers 3 and 4 have been drilled vertically and do not contribute significantly to the total injected volume to be representative; they are not represented here. Well 22 presents a particular profile where a drop in injection pressure is associated to an increase of the injection rate. It appears that index value, when higher that 2000 $m^3\ d^{-1}\ MPa{-}1$ (horizontal red line) generate seismicity for wells 13, 17, 22, 26, 27 and 28 (except for well 23) from 2014 January to April (see details in Section 5.1.2 and Fig. A2a).
Figure A6. Earthquakes location and migration at Rubiales at different periods: (a) 2013 July and pads position (red squares), (b) 2013 August, (c) 2013 September, (d) 2013 October–December, (e) 2014 January–March, (f) 2014 April–June, (g) 2014 July–September, (h) 2014 October–December, (i) 2015 January–June, (j) 2015 July–December, (k) 2016 January–June, (l) 2013 September (blue dots) and 2013 October–December (green dots). Hypocentres generated by Pad R6 in 2013 October–December appear to nucleate parallel and south of those recorded in 2013 July–September. This suggests the reactivation of a second fault or the same fault at greater depth.
Figure A7. Earthquakes depth evolution at Rubiales: (a) temporal evolution of the number of events by range of depth interval, and (b) temporal evolution of the percentage of events by range of depth interval.
Figure A8. Typical behaviour of well pad average injection pressure depending on their influence or lack of influence on seismicity: (a) Pad R5 and (b) Pad R6, respectively. Injection pressures at wells of Pad R5 are constant and merge while pressure at wells of Pad R6 pressure are widely distributed and unstable. We have observed that no seismicity is associated with injection at Pad R5 while intense seismicity migrates from Pad R6 in two directions (See Section 3.2 and Movie 1 available with the online version of the paper). Pressure at well R310 (Pad R6) is high and rather constant, as this well has

Downloaded from https://academic.oup.com/gji/article/223/2/777/5881935 by guest on 07 September 2020

been drilled vertically and its associated pressure pulse is less likely to affect a fault.

Figure A9. Injection Index values as a function of depth at Rubiales. Dots and crosses represent index values while color-shaded areas differentiate the pads. Both R6 and R7 are pads where injection generates seismicity. Index values for pad R6 increase as a function of depth with relatively low absolute values (within ± 700 $m^3\ d^{-1}\ MPa^{-1}$ from average). Six wells composing R7 drilled at similar depths present a variation of the injection Index far above average (500–2500 $m^3\ d^{-1}\ MPa^{-1}$). Wells at pads R1, R2, R3, R4, Pad R5 and R8, where injection does not generate much seismicity, are constrained to a specific depth (except for pads R1, R2 and R5).

Please note: Oxford University Press is not responsible for the content or functionality of any supporting materials supplied by the authors. Any queries (other than missing material) should be directed to the corresponding author for the paper.

Downloaded from https://academic.oup.com/gji/article/223/2/777/5881935 by guest on 07 September 2020